

Article

Facile Preparation of Highly Active CO₂ Reduction (001)TiO₂/Ti₃C₂T_x Photocatalyst from Ti₃AlC₂ with Less Fluorine

Jibai Li ¹, Kaining Li ^{1,2,*} , Qiuyan Tan ¹, Qin Li ¹, Jiajie Fan ³, Chao Wu ¹ and Kangle Lv ^{1,*} 

¹ College of Resources and Environment, South-Central Minzu University, Wuhan 430074, China; lijibai886@163.com (J.L.); tanqiuyan1@163.com (Q.T.); liqin0518@mail.scuec.edu.cn (Q.L.); wchao98514@163.com (C.W.)

² Division of Materials and Manufacturing Science, Graduate School of Engineering, Osaka University, Osaka 565-0871, Japan

³ School of Materials Science and Engineering, Zhengzhou University, Zhengzhou 450001, China; fanjiajie@zzu.edu.cn

* Correspondence: likaining082@hotmail.com (K.L.); lvkangle@mail.scuec.edu.cn (K.L.)

Abstract: To date, (001)TiO₂/Ti₃C₂T_x hybridized photocatalyst is usually prepared through the complicated treatment of Ti₃AlC₂ in the presence of corrosive fluorine with a molar ratio of nF:nTi of more than 20. To reduce the use of corrosive fluorine, herein, exploiting beyond the conventional method, we report a facile synthetic method for (001)TiO₂/Ti₃C₂T_x, elaborately using HF as both an etchant for Al elimination and a morphology control agent for the growth of (001)TiO₂ nanosheets, with a sharply diminished use of fluorine (nF:nTi = 4:1) and simplified operation procedures. After optimization, the resulting (001)TiO₂/Ti₃C₂T_x heterojunction exhibited markedly high photocatalytic activity with the CO₂ reduction rate of 13.45 μmol g⁻¹ h⁻¹, which even surpasses that of P25 (10.95 μmol g⁻¹ h⁻¹), while the photoelectron selectivity to CH₄ is approaching 92.84%. The superior photoactivity is interpreted as the fact that Ti₃C₂T_x with a lower work function induces photoinduced hole transfer and suppresses the charge recombination, thus facilitating the CO₂ multi-electron reduction. This study provides a novel and simple synthesis for (001)TiO₂/Ti₃C₂T_x towards sustainable energy transformations.

Keywords: MXenes; Ti₃C₂; (001) TiO₂; photocatalysis; CO₂ reduction



Citation: Li, J.; Li, K.; Tan, Q.; Li, Q.; Fan, J.; Wu, C.; Lv, K. Facile Preparation of Highly Active CO₂ Reduction (001)TiO₂/Ti₃C₂T_x Photocatalyst from Ti₃AlC₂ with Less Fluorine. *Catalysts* **2022**, *12*, 785. <https://doi.org/10.3390/catal12070785>

Academic Editors: Faryal Idrees and Faheem K. Butt

Received: 25 June 2022

Accepted: 14 July 2022

Published: 18 July 2022

Publisher's Note: MDPI stays neutral with regard to jurisdictional claims in published maps and institutional affiliations.



Copyright: © 2022 by the authors. Licensee MDPI, Basel, Switzerland. This article is an open access article distributed under the terms and conditions of the Creative Commons Attribution (CC BY) license (<https://creativecommons.org/licenses/by/4.0/>).

1. Introduction

TiO₂ is an extremely attractive candidate for photocatalysis, given the multiple advantages of low price, chemical durability, and ecological friendliness [1,2]. However, realistic applications of TiO₂ are restricted due to the rapid recombination of photogenerated electron-hole pairs. Therefore, numerous methods have been developed with the focus on the promotion of photoinduced charge transfer, such as loading co-catalyst [3,4], morphology modulation [5], and the construction of heterojunction [6–8]. Thereinto, loading co-catalyst on TiO₂ has hitherto been a satisfactory choice for improving its photoactivity and stability by accelerating the separation efficiency of photogenerated carriers. Nevertheless, the widespread utilization of noble-metal cocatalysts, such as Au and Pt, remains challenging for both high cost and scarcity. Hence, there is a considerable incentive to exploit cost-effective noble-metal-free cocatalysts for the enhancement of the TiO₂ photocatalytic performance.

MXenes, a new family of two-dimensional layered transition metal carbides, nitrides, or carbonitrides, possess a structural formula of M_{n+1}X_nT_x, where M refers to the early transition metal, X stands for carbon and/or nitrogen, T represents the surface functional groups (-O, -OH, -F), and n ranges from 1 to 3. Along with a mushrooming in the study of MXenes, up to now, more than 40 MXenes have been synthesized by selectively etching the metal layer from the precursor MAX phases [9]. Moreover, various syntheses for

different-dimension MXenes (e.g., quantum nanodots, nanorods, and nanosheets) have been reported [10]. Among all the MXenes, Ti_3C_2 is one of the most representative and prevalently studied materials in the field of photocatalysis, especially as a co-catalyst, because of the following reasons: (i) Its intrinsically metallic conductivity assures the efficient separation and transfer of photogenerated charge carriers from semiconductors [11–14]. (ii) The appropriate work function allows it to construct Schottky heterojunction with most semiconductors to alter their photoelectric properties [15,16]. As reported in previous work [17], $\text{Ti}_3\text{C}_2\text{T}_x$ can be coupled with (Ti, C) co-doped BiOBr to manipulate the carrier flow direction and achieve specific redox reactions via the elaborate Schottky heterojunction. (iii) The enormous surface functional groups favor the enhanced reactant adsorption capability [18].

In recent years, MXene-based materials receive considerable attention in photo/electrocatalysis. Amrillah et al. provided an insightful discussion on a series of syntheses for MXene-based and MXene-derived catalysts, including alcoholysis, hydrothermal treatment, and calcination process [10]. Typically, Ti_3C_2 is an ideal platform for the in situ growth of TiO_2 to prepare TiO_2 - Ti_3C_2 composite materials by partial oxidation. TiO_2 - Ti_3C_2 heterojunctions prepared by such in situ methods have intimate interfacial contact, which is conducive to the interface transfer of photoinduced electrons. To optimize the photocatalytic performance of TiO_2 / Ti_3C_2 catalysts, morphology engineering of TiO_2 (originated from partial oxidized Ti_3C_2) embedded in Ti_3C_2 has aroused the interest of material chemists [19]. In this way, plenty of TiO_2 nanostructures, including nanoparticles, nanoflowers, nanocrystals, and nanosheets, have been derived from Ti_3C_2 MXene [16,20–22]. Among them, (001) TiO_2 nanosheets stand out because they offer an excellent photoactivity that renders the TiO_2 / Ti_3C_2 heterojunction system attractive for many applications (photocatalytic environmental purification [16,22], photoelectrochemical detection [23], artificial photosynthesis of chemical fuels [24]).

To date, most of the synthesis methods for (001) TiO_2 / Ti_3C_2 have been carried out using at least two steps: (i) the raw material Ti_3AlC_2 was etched for Al layer elimination with HF, followed by washing to remove HF, and the Ti_3C_2 was finally obtained by drying; (ii) afterward, an additional fluorine source (e.g., NaBF) is added to regulate the in situ growth of (001) TiO_2 nanosheets on Ti_3C_2 by hydrothermal process [16,22]. For step (i), theoretically, to etch the Al layer of 1 mol Ti_3AlC_2 , 3 mol HF is needed according to the reaction equation [25]: $\text{Ti}_3\text{AlC}_2 + 3\text{HF} \rightarrow \text{Ti}_3\text{C}_2 + \text{AlF}_3 + 3/2\text{H}_2$. However, in those cases, the molar ratio of HF to Ti_3AlC_2 (nHF:n Ti_3AlC_2) is normally larger than 50:1, which is much more than the actual required amount. In fact, according to the study of Alhabeab et al., fewer HF (nHF:n Ti_3AlC_2 = 10:1) is enough to remove the Al layer of Ti_3AlC_2 [26]. It is well known that the large use of harmful HF is not environmentally friendly, thereby reducing the use of HF, meanwhile ensuring the elimination of the Al layer is rather significant. For step (ii), NaBF_4 is used as the shape-directing agent of (001) TiO_2 nanosheets. Additionally, its fluorine ion (F^-) plays an essential role in preparing (001) TiO_2 nanosheets, since F^- can combine with Ti atom to reduce the surface energy of (001) facet, resulting in the preferential growth of high-energy (001) facets during the growth process of TiO_2 crystal [27]. While many efforts have been devoted to fabricating (001) TiO_2 / Ti_3C_2 , some of the key challenges are still present that need to be addressed, especially the large usage of corrosive HF and the complexity of the operation.

Herein, a facile one-step hydrothermal method of (001) TiO_2 / $\text{Ti}_3\text{C}_2\text{T}_x$ composite was developed, as schematically illustrated in Figure 1. In this case, HF was delicately used as both an etchant for Al layer elimination of Ti_3AlC_2 and a morphology control agent providing F^- for the controlled growth of (001) TiO_2 nanosheets. In sharp contrast to traditional methods, we let the HF used in the etching process continue to participate in the hydrothermal reaction, rather than washing it off, so as to improve the utilization rate of HF and reduce its discharge. As a result, (i) the usage of HF is dramatically reduced; the molar ratio of F to Ti in the pristine materials of HF and Ti_3AlC_2 (nF:nTi) decreased from 21:1 to 4:1 as compared to the traditional synthesis method [16]. (ii) This work also simplifies the opera-

tion procedures, avoiding a series of processes, including washing, drying, and the addition of an extra morphology control agent. For detailed distinction, the experiment conditions and molar ratio ($nF:nTi$) for synthesizing $(001)TiO_2/Ti_3C_2T_x$ are summarized in Table S1. The optimized $(001)TiO_2/Ti_3C_2T_x$ exhibited superior photocatalytic CO_2 reduction activity, which was better than that of commercial P25 TiO_2 . It also showed remarkable selectivity for CH_4 production. The reason for the extraordinary photocatalytic performances may be the fact that $Ti_3C_2T_x$ with a lower work function induces the photogenerated hole transfer and suppresses the charge recombination, facilitating the CO_2 multi-electron reduction.

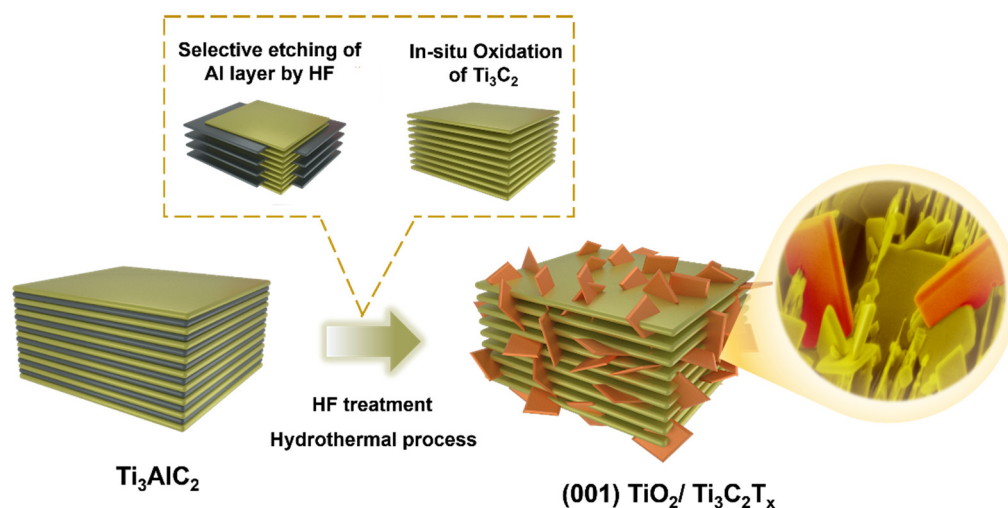


Figure 1. Schematic illustration of the synthesis procedure for $(001)TiO_2/Ti_3C_2T_x$ composite photocatalysts.

2. Results and Discussion

The phase structure of the sample was analyzed using X-ray diffraction (XRD) spectroscopy. As shown in Figure 2a, the diffraction peak of Ti_3AlC_2 MAX is consistent with that reported in the literature [12]. In comparison to Ti_3AlC_2 , the HF etching process causes the (104) diffraction peak at 39° to disappear in $Ti_3C_2T_x$, as well as the (002) and (004) diffraction peaks to shift towards lower angles, which are indications of Al layer elimination and increased layer spacing in the $Ti_3C_2T_x$ structure [28], as likewise evidenced by the observation of SEM images for both Ti_3AlC_2 and $Ti_3C_2T_x$ (Figure S2). For conciseness, the $TiO_2/Ti_3C_2T_x$ samples prepared by hydrothermal method are hereafter named TT- x , where x refers to the added volume (unit: mL) of the HF. All of the $TiO_2/Ti_3C_2T_x$ samples are well indexed to the peaks of both $Ti_3C_2T_x$ and anatase phase TiO_2 (JCPDS No. 21-1272), indicating that $TiO_2/Ti_3C_2T_x$ heterojunctions were successfully prepared (Figure 2a). However, there remains a faint (104) diffraction peak of Al at 39° for the TT-2 sample, which is mainly since the amount of HF added during the preparation was too small to etch the Al layer of Ti_3AlC_2 completely. When the amount of HF added was greater than 3 mL, the peak of Al fully disappeared in the corresponding position of the sample. Notably, the intensity of the diffraction peaks of TiO_2 decreased with the increasing HF addition higher than 5 mL. This is mainly because the excessive amount of HF will further etch the TiO_2 nanosheets and make them less crystalline. Among them, the crystallinity of TiO_2 in the $TiO_2/Ti_3C_2T_x$ composites prepared by the HF addition in the range of 3 mL to 5 mL was better.

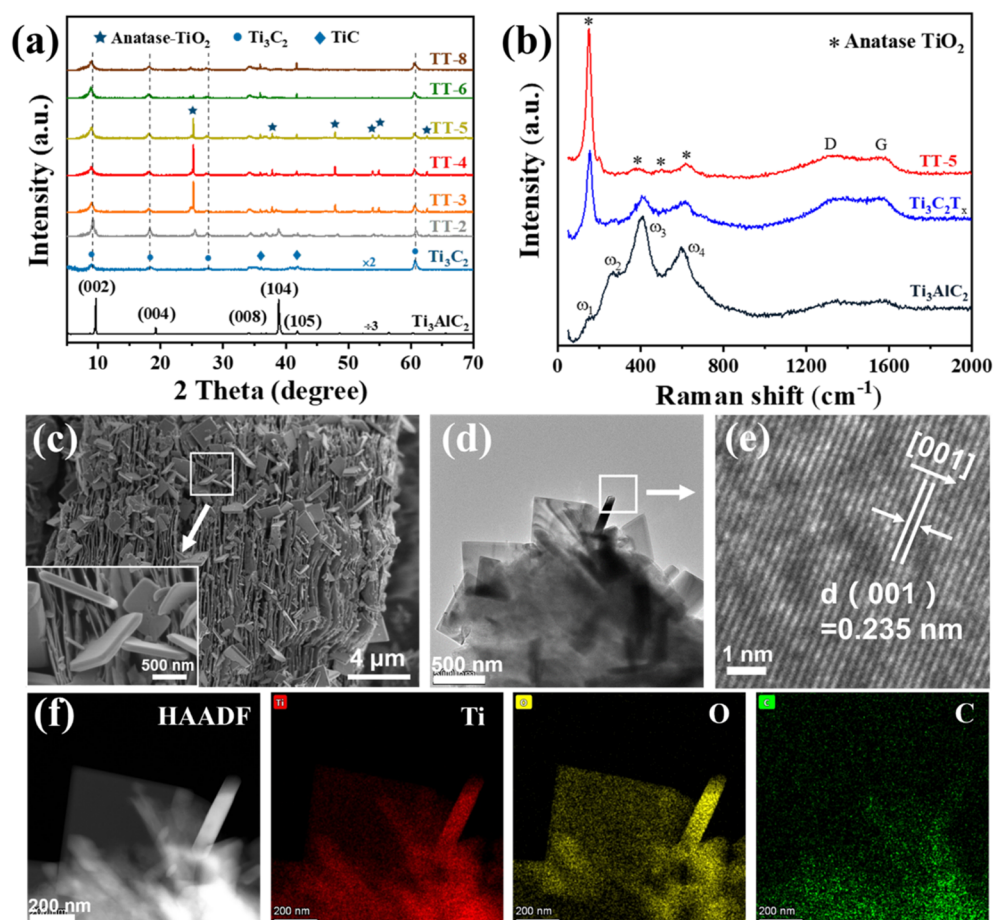


Figure 2. Evidence of the formation of (001) TiO₂/Ti₃C₂T_x complex samples. (a) XRD patterns of TiO₂/Ti₃C₂T_x composites with different usage of HF, Ti₃C₂T_x and Ti₃AlC₂. (b) Raman spectra of TT-5, Ti₃C₂T_x and Ti₃AlC₂. (c) FESEM and (d) TEM image of TT-5, the inset of c shows TiO₂ nanosheets embedding in layered Ti₃C₂T_x substrate. (e) HRTEM image showing the lattice of the TiO₂ with the exposed (001) plane in TT-5. (f) HAADF STEM image and the corresponding EDS elemental maps of Ti, O and C of TT-5.

In addition to XRD, Raman spectra were used to reveal the constituents of the as-prepared samples, yielding similar results. As shown in Figure 2b, Ti₃AlC₂ contains several characteristic bands that appeared at ca. 169, 268, 411, and 598 cm⁻¹, which are associated with the ω₁, ω₂, ω₃, and ω₄ Raman-active phonon vibration modes, respectively, while the two peaks between 1000 and 1800 cm⁻¹ (D and G band) are referred to the stretching vibrations of graphitic carbon [12,22]. For the other two samples, the Ti₃C₂T_x sample showed the expected Raman vibrational modes [15,29]. Compared to the Ti₃C₂T_x sample, the TT-5 sample displayed an ascending Raman signal at 150 cm⁻¹ (E_g), together with three other peaks at 393 cm⁻¹ (B_{1g}), 507 cm⁻¹ (A_{1g}), 630 cm⁻¹ (E_g), which are originated from anatase (001)TiO₂ [12,30]. Besides, the D- and G-modes peaks of Ti₃C₂T_x were also observed clearly in TT-5. Reasonably, both XRD and Raman results confirm the transformation of Ti₃C₂T_x to TiO₂ during hydrothermal treatment.

Another direct piece of evidence for the successful preparation of TiO₂/Ti₃C₂T_x is provided by the morphology and microstructure observation via field emission scanning electron microscopy (FESEM) and high-angle annular dark field scanning transmission electron microscope (HAADF-STEM). The most striking feature of the typical heterojunction is the existence of TiO₂ nanosheets embedded in Ti₃C₂T_x that are deliberately created using a fluorine source (HF) under the hydrothermal process. This characteristic is directly observed with FESEM (Figure 2c), showing square TiO₂ nanosheets with a thickness of 130 nm embedded in the layered Ti₃C₂T_x. The TEM image (Figure 2d) of TiO₂/Ti₃C₂T_x

displays several square thin nanosheets on a substrate, and its partially enlarged image (Figure 2e) shows the obvious lattice spacing of 0.235 nm, which is identified for the TiO₂ (001) plane. Usually, the growth rate of crystals is exponentially related to the surface energy [31]. During the growth of TiO₂ nuclei, the (001) planes with high surface energy (0.90 J/m²) decrease rapidly, and the TiO₂ nanocrystals evolve spontaneously into a truncated bipyramidal structure dominated by stable (101) facets because of their low surface energy (0.44 J/m²) [32]. It is worth noting that modifying the surface adsorption species of the crystal can change the surface energy, exposing specific highly active facets of the crystal. F is a species with the affinity for Ti atoms so that it can bind Ti atoms and reduce the surface energy of the (001) facets, making them more stable than the (101) facets during the anatase TiO₂ crystal growth process [27,33]. Therefore, in our case, the absorbed F atom functioned as a capping agent to modify the surface energy of (001) facets of TiO₂, resulting in exceptional stabilization. Furthermore, the elemental distribution in the composite was visualized by STEM-energy-dispersive X-ray spectroscopy (EDS) mapping analysis (Figure 2f). By focusing on an area containing square sheets with lying and standing positions, it is clearly revealed that the distributions of Ti atoms and O atoms are perfectly coincided with the square region, verifying the formation of TiO₂ nanosheet structure. Therefore, it can be concluded that the (001)TiO₂/Ti₃C₂T_x has been successfully prepared.

As evidenced above, after HF pretreatment and hydrothermal process for precursor Ti₃AlC₂, the Al layer has been removed and the TiO₂/Ti₃C₂T_x heterojunction was formed. To further confirm the changes in the surface composition of the prepared samples Ti₃AlC₂, TT-5, and TT-5-u (the sample pretreated with 5 mL HF but without hydrothermal treatment) at different stages in synthesis, XPS measurements were carried out. As a consequence of the Al layer removal, Al 2s and 2p peaks in Ti₃AlC₂ disappeared in TT-5 and TT-5-u, which can be observed via the XPS survey spectra (Figure S3). The comparison of the high-resolution Ti 2p spectrum between TT-5 and TT-5-u is shown in Figure 3a,d. For TT-5, the Ti 2p spectrum can be fitted by seven components located at 454.8, 456.3, 456.5, 459.4, 461.3, 462.6, and 465.0 eV, which are attributed to Ti-C (454.8 eV and 461.3 eV), Ti-X (456.3 eV) (substoichiometric TiC_x (x < 1) or titanium oxycarbides), Ti³⁺ (456.5 eV and 462.6 eV), and TiO₂ (459.4 eV and 465.0 eV) [12,16,22]. In comparison to TT-5-u, the TT-5 sample shows two more peaks of TiO₂ (459.4 eV and 465.0 eV) and the fade of the other Ti species, demonstrating the gradual transformation from Ti₃C₂T_x to TiO₂. Furthermore, the C 1s spectrum (Figure 3b) of TT-5 exhibited several distinct peaks at 288.8, 286.4, 284.8, 282.5, and 281.9 eV, corresponding to C-F, C-O, C-C, C-Ti-O, and Ti-C, respectively [16,22,34]. Apparently, C-F is derived from HF; Ti-C and C-C originate from Ti₃C₂T_x and adventitious carbon, respectively. It is noteworthy that the TT-5 showed a new C-Ti-O peak at 282.5 eV as compared with TT-5-u (Figure 3e), demonstrating that the TiO₂/Ti₃C₂T_x heterojunction is linked by a C-Ti-O bond. The O 1s spectrum of TT-5-u is fitted by two components located at 532.18 and 530.0 eV (Figure 3f), which are corresponding to Ti-OH, Ti-O [35]. After hydrothermal treatment, the Ti-O intensity of TT-5 significantly increased as compared to Ti-OH (Figure 3c), which suggests the existence of TiO₂. The XPS results verify the successful preparation of the TiO₂/Ti₃C₂T_x heterojunction, which is well consistent with the results of XRD, Raman, and EDS analyses.

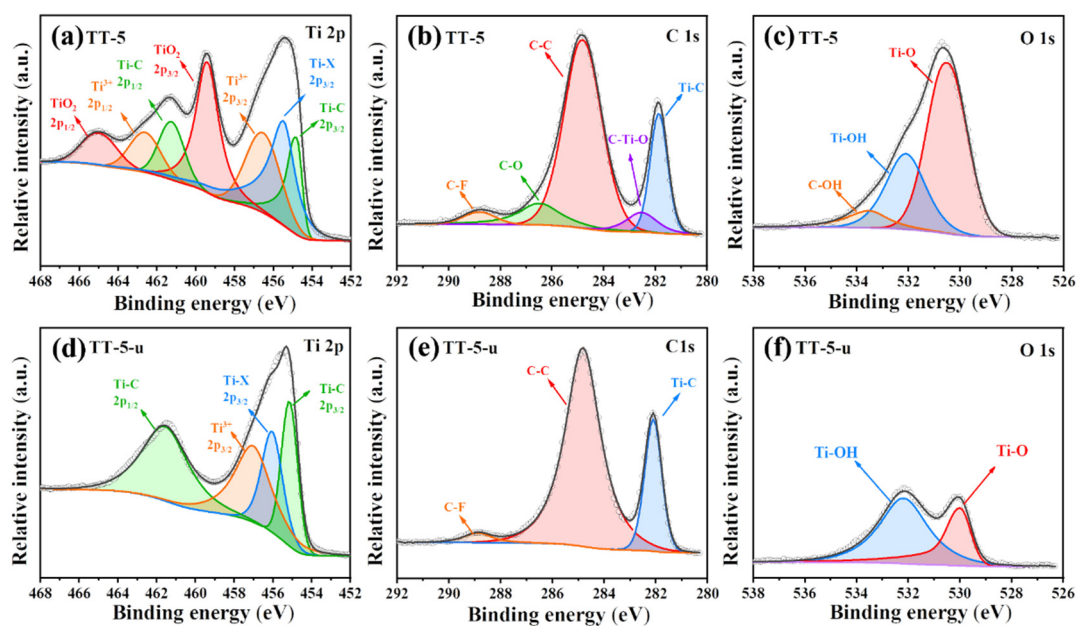


Figure 3. High-resolution XPS spectra for Ti 2p (a,d), C 1s (b,e) and O 1s (c,f) of TT-5 (a–c) and TT-5-u (d–f).

The photocatalytic activity of the samples was evaluated by photocatalytic CO₂ reduction in a gas-solid reaction system under simulated solar light. Mild conditions were kept without using any photosensitizer or organic sacrificial reagents. Methane (CH₄) and carbon monoxide (CO) are generated as the predominant products via the two-electron and eight-electron reduction processes, respectively (Figure 4a). Ti₃C₂T_x with metallic properties is generally not photocatalytically active [28]. However, a weak CO₂ photoreduction activity of Ti₃C₂T_x was detected here, resulting from the TiO₂ (partial oxidation Ti₃C₂T_x) during storage or light exposure. As for the other samples, the photoactivity showed a trend to increase and then decline as the increasing addition of HF. From TT-2 to TT-5, the photoactivity gradually enhanced due to the increase in (001)TiO₂ nanosheets on Ti₃C₂T_x, which is consistent with the trend seen in the XRD and SEM results (Figures 2a and S4). Besides, for nitrogen adsorption-desorption isotherms and corresponding pore-size distribution analysis (Figure S5 and Table S2), TT-5 shows larger surface area and more micropores (<2 nm) as compared to TT-2, which may favor the adsorption of CO₂ gas molecules. However, following adding excessive HF, the TiO₂ may further be etched (as shown in Figure S4), resulting in a decrease in the photoactivity for TT-6 and TT-8. The results suggest that there is an optimum amount (5 mL) of HF in the synthesis of TiO₂/Ti₃C₂T_x for achieving high photocatalytic CO₂ reduction rates. Among all the samples, TT-5 exhibited the best CO₂ photoreduction rate of 13.45 μmol g^{−1} h^{−1} (10.28 μmol g^{−1} h^{−1} for CH₄ and 3.17 μmol g^{−1} h^{−1} for CO), which was higher than that of P25 TiO₂ (10.95 μmol g^{−1} h^{−1}). Note that methane was not detected for commercial P25, while TT-5 was up to 92.84% methanogenic selectivity (Figure 4b). As reported previously, the existence of Ti₃C₂ favors the selectivity for photocatalytic CO₂–CH₄ conversion [36,37]. Combining the reported studies and above experimental results, the reason for the extraordinary selectivity for CH₄ production could be interpreted as Ti₃C₂ with lower work function induces the photo-generated hole transfer and suppresses the charge recombination, facilitating the CO₂ multi-electron reduction.

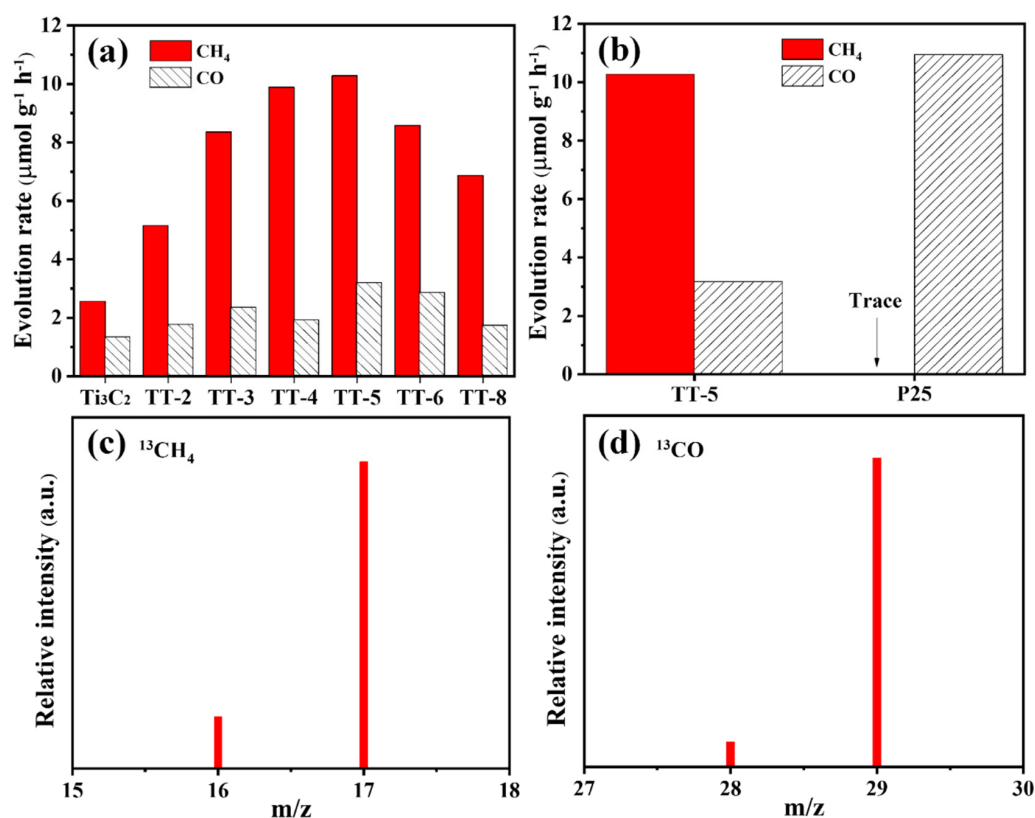


Figure 4. (a) Photocatalytic activities of CO₂ reduction over the prepared samples. (b) Comparison of product selectivity for TT-5 and P25. (c,d) Mass patterns of produced CH₄ ($m/z = 17$) and CO ($m/z = 29$) over TT-5 in photocatalytic ¹³CO₂ reduction.

A series of control experiments were conducted to reveal the source of reduction products; the results are shown in Figure S6. The product concentration is below the limit of detection when the experiments were carried out in the absence of catalyst or irradiation or in Ar, proving that the detectable CO and CH₄ were derived from photocatalytic CO₂ reduction over (001)TiO₂/Ti₃C₂T_x. To further disclose the origin of the products, an isotopically labeled ¹³CO₂ experiment was performed. As shown in Figure 4c,d, the strong signals were observed at $m/z = 17$ and $= 29$, which were attributed to ¹³CH₄ and ¹³CO, respectively. This result further confirms that the reduction products indeed originate from the CO₂ photoreduction rather than from the impurity or the sample.

With efforts to acquire an in-depth understanding of the reaction intermediates in CO₂ photoreduction for TT-5, in situ diffuse reflectance infrared Fourier transform spectroscopy (DRIFTS) was performed (Figure 5). Obviously, various peaks can be observed during the photocatalytic reaction that corresponds to the formation of carbonate species, in which CO₃²⁻ and HCO₃⁻ are generated from CO₂ and -OH [38]. The peaks at 1868, 1844, 1828, 1792, 1698, 1684, 1576, and 1558 cm⁻¹ were attributed to HCOO [12,28,39], while the band for COOH* was located at 1569 cm⁻¹ [40]; they might serve as possible intermediates for CO production. Furthermore, the peaks at 1772, 1750, 1716, 1457, and 1419 cm⁻¹ belong to HCHO [12,28,41], and the peak at 1734 cm⁻¹ originates from CH₃O [41], both of which are important intermediate species for the production of CH₄. Notably, the signal of CH₄ was undetectable on DRIFT spectra, as it is a non-polar molecule. Therefore, the CO₂ photoconversion process could be deduced as follows: CO₂ molecules are firstly adsorbed on the surface of the TT-5 sample and reacted with H⁺ dissociated from H₂O to form COOH* (CO₂* + e⁻ + H⁺ → COOH*). Then, COOH* transformed to CO* by a protonation process (COOH* + e⁻ + H⁺ → CO* + H₂O) [40,42]. One part of the adsorbed CO* is released to form gaseous CO (CO* → CO); more importantly, the other part of CO* continues to participate in the reduction reaction to form HCHO* and CH₃O* (CO* + 2e⁻ + 2H⁺ →

HCHO^* ; $\text{HCHO}^* + e^- + \text{H}^+ \rightarrow \text{CH}_3\text{O}^*$). Eventually, the CH_4 production could be achieved by the further protonation of CH_3O^* ($\text{CH}_3\text{O}^* + 3e^- + 3\text{H}^+ \rightarrow \text{CH}_4\uparrow + \text{H}_2\text{O}$) [43].

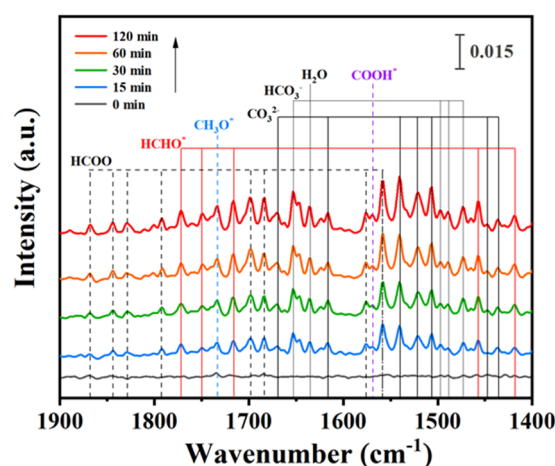


Figure 5. In situ DRIFTS spectra of photocatalytic CO_2 reduction on TT-5.

Furthermore, considering that the separation and migration of photoinduced electron-hole pairs play an important role in achieving the enhancement of photocatalytic efficiency, the transient photocurrent response test was performed. As shown in Figure 6a, the anode photocurrent increases during irradiation and declines without irradiation. It can clearly be seen that TT-5 exhibited improved photocurrent responses compared with other samples, suggesting the efficient separation of the charge carriers in the composites of TT-5. Notably, the rapid decay characteristic of P25 could be assigned to fast electron-hole recombination kinetics due to the absence of $\text{Ti}_3\text{C}_2\text{T}_x$ with high conductivity [12,44]. For the others, their photocurrent is relatively stable, because the presence of $\text{Ti}_3\text{C}_2\text{T}_x$ slows down the recombination rate of photogenerated carriers, which is beneficial for the multi-electron reduction of CO_2 ($\text{CO}_2 + 8\text{H}^+ + 8e^- \rightarrow \text{CH}_4\uparrow + 2\text{H}_2\text{O}$).

In an effort to better understand the pathway of interfacial charge transfer between (001) TiO_2 nanosheets (synthesized according to our previous report [45]) and $\text{Ti}_3\text{C}_2\text{T}_x$, the work functions (W_{sample}) of them were studied via Kelvin probe using a gold mesh as the reference. Specifically, the W_{sample} is calculated by Equation (1) [46]:

$$W_{\text{sample}} = W_{\text{probe}} + e \cdot \text{CPD}_{\text{sample}} \quad (1)$$

where $\text{CPD}_{\text{sample}}$ is the contact potential difference (CPD) of the given sample, which was measured by the Kelvin probe; W_{probe} represents the work function of the gold mesh (≈ 4.25 eV); and e is the electronic charge. Based on the probed CPD results (Figure 6b), the W of (001) TiO_2 nanosheets and $\text{Ti}_3\text{C}_2\text{T}_x$ are calculated to be 4.66 and 4.42 eV, respectively (Figure 6c). Accordingly, the Fermi levels (E_f) of the samples are determined via the conversion formulas (Equations (2)–(4)) [28], as shown below:

$$E_{f,\text{vac}} = E_{\text{vac}} - W_{\text{sample}} \quad (2)$$

$$E_f(\text{vs.SHE, pH0}) = -4.5 \text{ V} - E_{f,\text{vac}} \quad (3)$$

$$E_f(\text{vs.SHE, pH7}) = E_f(\text{vs.SHE, pH0}) - 0.059 \text{ pH} \quad (4)$$

where the $E_{f,\text{vac}}$ represents the Fermi levels of the samples at the vacuum level, and E_{vac} is the energy of a stationary electron at the vacuum level (regarded as 0 eV). Thus, the E_f of $\text{Ti}_3\text{C}_2\text{T}_x$ and TiO_2 are calculated to be -0.49 and -0.25 eV (vs. SHE at pH = 7), respectively. Obviously, the Fermi energy level of $\text{Ti}_3\text{C}_2\text{T}_x$ is more negative than that of (001) TiO_2 nanosheets (i.e., the work function of $\text{Ti}_3\text{C}_2\text{T}_x$ is lower than that of (001) TiO_2), and thus the photogenerated holes rather than electrons of TiO_2 nanosheets are trapped by $\text{Ti}_3\text{C}_2\text{T}_x$.

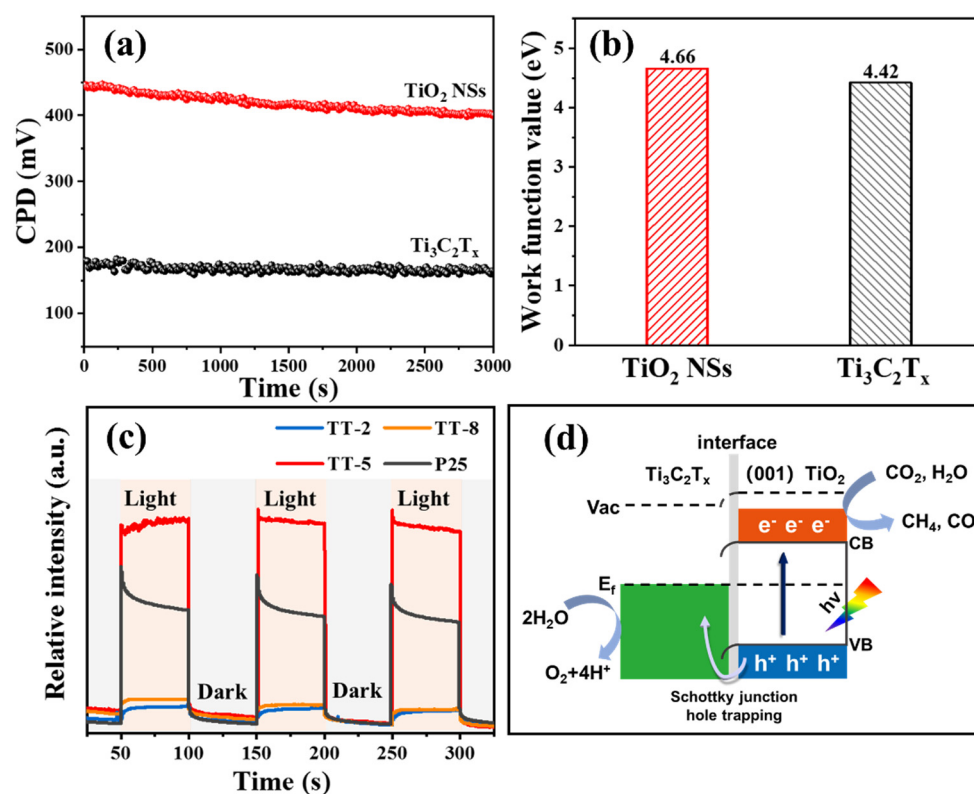


Figure 6. (a) CPD values measured by Kelvin probe and (b) the corresponding work functions of TiO₂ nanosheets and Ti₃C₂T_x sample. (c) Photocurrent density of TT-2, TT-8, TT-5 and P25 sample. (d) Schematic for the mechanism of photocatalytic CO₂ reduction on (001) TiO₂/Ti₃C₂T_x.

Based on the above experimental results, we inferred the mechanism of (001) TiO₂/Ti₃C₂T_x for photocatalytic CO₂ reduction (Figure 6d). Under illumination, the electrons on the valence band of (001)TiO₂ nanosheets are excited to the conduction band, and these photoelectrons gathered on the conduction band react with the adsorbed CO₂ to generate CH₄ and CO via the photocatalytic process. Because of the differences in work function for (001)TiO₂ nanosheets and Ti₃C₂T_x with metallic properties, a Schottky barrier could be formed at the interface of (001)TiO₂ and Ti₃C₂T_x [16,22], which would promote the holes rather than electrons transfer to Ti₃C₂T_x, while enabling the accumulation of electrons on TiO₂. Undoubtedly, this is favorable for the efficiently multi-electron CO₂ photoreaction.

3. Experimental Procedures

3.1. Chemicals

All the chemicals were of analytic grade and used as received. Deionized (DI) water used in this research was from local sources. Ti₃AlC₂ powder was supplied by 11 Technology Co., Ltd. (Changchun, China). Hydrofluoric acid (HF), sulfuric acid (H₂SO₄), and sodium bicarbonate (NaHCO₃) were obtained from Sinopharm Chemical Reagent Co., Ltd. (Shanghai, China).

3.2. Sample Preparation

Preparation of Ti₃C₂T_x: Ti₃C₂T_x was prepared by an HF-etching method. In detail, 1 g Ti₃AlC₂ powder was slowly put into the aqueous HF solution (40 wt%) under magnetic stirring for 24 h to eliminate the Al layer. Then, the black suspension was filtered and washed with distilled water until the pH of the filtrate was about 7. After drying at 60 °C under vacuum for 12 h, the Ti₃C₂T_x powder was obtained.

Preparation of (001) TiO₂/Ti₃C₂T_x: (001) TiO₂/Ti₃C₂T_x composite photocatalysts were synthesized by a one-step hydrothermal method. Typically, 2 g Ti₃AlC₂ powder was slowly

added to HF solution (5 mL, 40 wt%) and kept agitating at room temperature for 24 h in order to remove the Al layer. Then, distilled water was directly added to the above suspensions to a total volume of 120 mL. After sonicating for 10 min, the homogeneous mixture was sealed into a 200 mL Teflon-lined autoclave with a stainless steel jacket for a hydrothermal process at 180 °C for 12 h, in which HF was delicately used as both an etchant for Ti_3AlC_2 and a morphology control agent for the growth of (001) TiO_2 nanosheets on $\text{Ti}_3\text{C}_2\text{T}_x$. After natural cooling, the precipitate was collected by filtration, washed thoroughly with distilled water until the pH of the filtrate turned to 7, and dried at 60 °C. Subsequently, the (001) $\text{TiO}_2/\text{Ti}_3\text{C}_2\text{T}_x$ was obtained and labeled as TT-5 (5 mL HF) for short.

Similarly, a serial of composites was synthesized by varying the usage of HF under other identical conditions, and the acquired samples were named TT- x ($x = 2, 3, 4, 5, 6$, and 8), where x represents the usage (unit: mL) of HF. To study the transformation process of Ti_3AlC_2 to (001) $\text{TiO}_2/\text{Ti}_3\text{C}_2\text{T}_x$, samples pretreated with 5 mL HF but without hydrothermal process were collected and labeled TT-5-u.

3.3. Characterization

The X-ray diffraction (XRD) patterns of the samples were recorded on an X-ray diffractometer (D8 ADVANCE Bruker, Karlsruhe, Germany) with Cu $K\alpha$ radiation at a scan rate of $0.02^\circ \text{ s}^{-1}$. Raman spectra were collected through a Raman spectroscopy (DXR2 XI, Thermo Fisher, Waltham, MA, USA) with an excitation wavelength of 633 nm. The morphology and microstructure of the samples were analyzed using a field emission scanning electron microscope (FESEM, SU8010 Hitachi, Tokyo, Japan) and high-angle annular dark-field scanning/transmission electron microscopy (HAADF-STEM, Talos F200S, Thermo Scientific, Waltham, MA, USA), respectively. X-ray photoelectron spectroscopy (XPS) measurements were performed using a VG Multilab 2000 XPS system (Thermo VG Scientific, London, UK) to obtain information related to the surface chemical state and composition of the sample. All the spectra were calibrated to the C 1s peak at 284.8 eV. The UV-vis diffuse reflectance spectra (DRS) were obtained with a UV-vis spectrophotometer (UV2600, Shimadzu, Kyoto, Japan) using BaSO_4 as the reference standard. The Brunauer-Emmett-Teller (BET) surface area and pore size distribution data of the samples were analyzed using a nitrogen adsorption apparatus (ASAP-2020, Micromeritics, Norcross, GA, USA). The samples were degassed at 175 °C for 4 h before N_2 adsorption measurement. A Kelvin probe apparatus (Instytut Fotonowy, Cracow, Poland) with a sensitivity of 1 mV was utilized to determine the contact potential difference (CPD) of the samples with a gold mesh Kelvin probe as the reference. Surface work function (W) was monitored using an LED lamp as a light source in conjunction with a monochromator. In situ FTIR spectra were measured on a Bruker Tensor II FTIR spectrometer (Bruker, Karlsruhe, Germany).

3.4. Electrochemical Measurements

Electrochemical characterization for transient photocurrent responses (TPR) was conducted on an electrochemical analyzer (CHI 760e, CH Instruments, Shanghai, China). Pt wire, Ag/AgCl (saturated KCl), and 0.4 M Na_2SO_4 solution were functioned as the counter electrode, reference electrode, and electrolyte, respectively. For the working electrode, 30 mg of catalyst was ground in 1 mL water/absolute ethanol mixed solvent ($v/v = 1/1$) and 30 μL of Nafion solution to make a slurry, which was coated onto indium tin oxide (ITO) conductive glass with an exposed area of 1 cm^2 after ultrasonic dispersion. A 365 nm LED (3 W, Shenzhen Lamplic, Shenzhen, China) was used as the light source.

3.5. Photocatalytic CO_2 Reduction and Isotope-Labeling Measurement

The photocatalytic CO_2 reduction of the samples was conducted in a glass automatic online gas analysis system (Labsolar-6A, Beijing, China) (Figure S1a). The light source was a 300 W xenon lamp (PLS-SXE300+, Beijing, China). The photocatalytic activity test was carried out in three main steps: coating catalyst, in situ CO_2 production, and the occurrence of the CO_2 photocatalytic reduction. (1) Coating catalyst: 30 mg of the photocatalyst was

dispersed in 15 mL distilled water to form a suspension, which was then transferred to a petri dish ($\phi = 60$ mm). After drying, the catalyst film was deposited on the bottom of the dishes. (2) In situ CO₂ generation: 2.1 g of NaHCO₃ powder was placed on the bottom of a homemade double-neck reactor, and the coated dish in (1) was supported in the reactor using a quartz tripod (Figure S1b). Before illumination, the photocatalytic system was vacuumed to exclude the air. Finally, 7 mL of H₂SO₄ (2 M) was injected into the reactor to react with NaHCO₃ for generating CO₂ and H₂O vapor within the reactor. (3) CO₂ photoreduction (Figure S1c): After adsorption equilibrium, a 300 W xenon lamp (PLS-SXE300+, Perfect Light) was used as the light source to initiate the photocatalytic reaction. The concentration of the CO₂ reduction products was analyzed by gas chromatography (GC-2014, Shimadzu, Kyoto, Japan) with FID and TCD detectors. For determining the carbon source of the reduction products, ¹³CO₂ isotope labeling experiment was carried out under the same conditions as the above-mentioned CO₂ reduction test, except for the substitute of NaH¹²CO₃ using NaH¹³CO₃ (SHANGHAI ZZBIO Co., Ltd., Shanghai, China). The gas products were verified by a mass spectrometer (MS, HPR-20, Hiden Analytical, Warrington, UK). The electron selectivity for CH₄ production during the photocatalytic CO₂ reduction process is evaluated using the following equation [47]: CH₄ selectivity (%) = $[(8n(\text{CH}_4)) / ((8n(\text{CH}_4) + 2n(\text{CO})) \times 100$, CO selectivity (%) = $[(2n(\text{CO})) / ((8n(\text{CH}_4) + 2n(\text{CO})) \times 100$, where $n(\text{CH}_4)$ and $n(\text{CO})$ denote the number of moles of CH₄ and CO, respectively.

4. Conclusions

In summary, a facile one-step hydrothermal approach of (001)TiO₂/Ti₃C₂T_x composite was developed, where HF was delicately used as both an etchant for Ti₃AlC₂ and a morphology control agent for TiO₂ nanosheets. This method simultaneously addressed the issues of the large usage of HF and complex operation procedure. Furthermore, by tailoring the HF amount within a narrow range, the morphology of TiO₂ nanosheets could be purposefully manipulated. The optimized sample (TT-5) shows a superior photoactivity with a CO₂ reduction rate of 13.45 $\mu\text{mol g}^{-1} \text{h}^{-1}$, as well as a CH₄ production selectivity of 92.84%. The excellent photocatalytic performance is mainly since purposeful spatial isolation of photogenerated charge carriers induced by Ti₃C₂T_x dramatically improves the electron density of TiO₂, thereby facilitating the CO₂ multi-electron reduction of (001)TiO₂/Ti₃C₂T_x heterojunction. This work may provide an easy and novel approach to fabricating highly efficient MXene-derived composites for sustainable energy conversion.

Supplementary Materials: The following supporting information can be downloaded at: <https://www.mdpi.com/article/10.3390/catal12070785/s1>, Figure S1: Photocatalytic CO₂ reduction device (a), in situ CO₂ production (b), CO₂ photoreduction reaction (c); Figure S2: SEM image of Ti₃AlC₂ (a) and Ti₃C₂ (b), showing that the morphology of bulk Ti₃AlC₂ changed to accordion-like Ti₃C₂T_x, as a consequence of the eliminated Al layer via HF etching; Figure S3: X-ray photoelectron spectroscopy (XPS) survey spectra (a) and high-resolution XPS spectra of Al 2p (b) of Ti₃AlC₂, TT-5-u and TT5; Figure S4: SEM images of TiO₂/Ti₃C₂T_x samples prepared with different usage of HF; Figure S5: Nitrogen adsorption/desorption isotherms and the corresponding pore-size distribution curves (inset) of the TT-2, TT-5 and TT-8 samples; Figure S6: The control experiments of photocatalytic CO₂ reduction performance over TT-5 under altered conditions; Table S1: Synthesis conditions of (001)TiO₂/Ti₃C₂T_x composites; Table S2: BET surface area and the corresponding pore volume and pore size of samples [48–51].

Author Contributions: Conceptualization, K.L. (Kangle Lv); methodology, K.L. (Kangle Lv); formal analysis, J.L., K.L. (Kaining Li), Q.T., Q.L., C.W. and K.L. (Kangle Lv); investigation, J.L. and K.L. (Kaining Li); resources, K.L. (Kangle Lv); data curation, J.L. and K.L. (Kaining Li); writing—original draft preparation, J.L. and K.L. (Kaining Li); Visualization, C.W.; writing—review and editing, Q.L., J.F. and K.L. (Kangle Lv); supervision, project administration and funding acquisition, K.L. (Kangle Lv). All authors have read and agreed to the published version of the manuscript.

Funding: This work was supported by the National Natural Science Foundation of China (51672312, 21972171 and 52073263) and the Fundamental Research Funds for the Central Universities, South-Central Minzu University (CZP22001).

Data Availability Statement: Not applicable.

Conflicts of Interest: The authors declare no conflict of interest.

References

1. Li, W.; Elzatahry, A.; Aldhayan, D.; Zhao, D. Core-Shell Structured Titanium Dioxide Nanomaterials for Solar Energy Utilization. *Chem. Soc. Rev.* **2018**, *47*, 8203–8237. [[CrossRef](#)] [[PubMed](#)]
2. Gong, H.; Wang, L.; Zhou, K.; Zhang, D.; Zhang, Y.; Adamaki, V.; Sergejevs, A.; Bowen, C. Improved Photocatalytic Performance of Gradient Reduced TiO₂ Ceramics with Aligned Pore Channels. *Adv. Powder Mater.* **2022**, *1*, 100025. [[CrossRef](#)]
3. Xu, F.; Meng, K.; Zhu, B.; Liu, H.; Xu, J.; Yu, J. Graphdiyne: A New Photocatalytic CO₂ Reduction Cocatalyst. *Adv. Funct. Mater.* **2019**, *29*, 1904256. [[CrossRef](#)]
4. Meng, A.; Zhang, L.; Cheng, B.; Yu, J. Dual Cocatalysts in TiO₂ Photocatalysis. *Adv. Mater.* **2019**, *31*, 1807660. [[CrossRef](#)] [[PubMed](#)]
5. Sajan, C.P.; Wageh, S.; Al-Ghamdi, A.A.; Yu, J.; Cao, S. TiO₂ Nanosheets with Exposed {001} Facets for Photocatalytic Applications. *Nano Res.* **2016**, *9*, 3–27. [[CrossRef](#)]
6. Xu, F.; Meng, K.; Cheng, B.; Wang, S.; Xu, J.; Yu, J. Unique S-Scheme Heterojunctions in Self-Assembled TiO₂/CsPbBr₃ Hybrids for CO₂ Photoreduction. *Nat. Commun.* **2020**, *11*, 4613. [[CrossRef](#)]
7. Low, J.; Dai, B.; Tong, T.; Jiang, C.; Yu, J. In Situ Irradiated X-ray Photoelectron Spectroscopy Investigation on a Direct Z-scheme TiO₂/CdS Composite Film Photocatalyst. *Adv. Mater.* **2019**, *31*, 1802981. [[CrossRef](#)] [[PubMed](#)]
8. Zhang, Z.; Zhang, Y.; Han, X.; Guo, L.; Wang, D.; Lv, K. Assembly of CaIn₂S₄ on Defect-Rich BiOCl for Acceleration of Interfacial Charge Separation and Photocatalytic Phenol Degradation via S-Scheme Electron Transfer Mechanism. *Catalysts* **2021**, *11*, 1130. [[CrossRef](#)]
9. Naguib, M.; Barsoum, M.W.; Gogotsi, Y. Ten Years of Progress in the Synthesis and Development of MXenes. *Adv. Mater.* **2021**, *33*, 2103393. [[CrossRef](#)]
10. Amrillah, T.; Hermawan, A.; Alviani, V.N.; Seh, Z.W.; Yin, S. MXenes and Their Derivatives as Nitrogen Reduction Reaction Catalysts: Recent Progress and Perspectives. *Mater. Today Energy* **2021**, *22*, 100864. [[CrossRef](#)]
11. Ran, J.; Gao, G.; Li, F.T.; Ma, T.Y.; Du, A.; Qiao, S.Z. Ti₃C₂ MXene Co-Catalyst on Metal Sulfide Photo-Absorbers for Enhanced Visible-Light Photocatalytic Hydrogen Production. *Nat. Commun.* **2017**, *8*, 13907. [[CrossRef](#)] [[PubMed](#)]
12. Low, J.; Zhang, L.; Tong, T.; Shen, B.; Yu, J. TiO₂/MXene Ti₃C₂ Composite with Excellent Photocatalytic CO₂ Reduction Activity. *J. Catal.* **2018**, *361*, 255–266. [[CrossRef](#)]
13. Chen, L.; Ye, X.; Chen, S.; Ma, L.; Wang, Z.; Wang, Q.; Hua, N.; Xiao, X.; Cai, S.; Liu, X. Ti₃C₂ MXene Nanosheet/TiO₂ Composites for Efficient Visible Light Photocatalytic Activity. *Ceram. Int.* **2020**, *46*, 25895–25904. [[CrossRef](#)]
14. Li, W.; Zhuang, C.; Li, Y.; Gao, C.; Jiang, W.; Sun, Z.; Qi, K. Anchoring Ultra-Small TiO₂ Quantum Dots onto Ultra-Thin and Large-Sized Mxene Nanosheets for Highly Efficient Photocatalytic Water Splitting. *Ceram. Int.* **2021**, *47*, 21769–21776. [[CrossRef](#)]
15. Li, Z.; Huang, W.; Liu, J.; Lv, K.; Li, Q. Embedding CdS@Au into Ultrathin Ti_{3-x}C_{2-y} to Build Dual Schottky Barriers for Photocatalytic H₂ production. *ACS Catal.* **2021**, *11*, 8510–8520. [[CrossRef](#)]
16. Peng, C.; Yang, X.; Li, Y.; Yu, H.; Wang, H.; Peng, F. Hybrids of Two-Dimensional Ti₃C₂ and TiO₂ Exposing {001} Facets toward Enhanced Photocatalytic Activity. *ACS Appl. Mater. Interfaces* **2016**, *8*, 6051–6060. [[CrossRef](#)]
17. Hermawan, A.; Hasegawa, T.; Asakura, Y.; Yin, S. Enhanced Visible-Light-Induced Photocatalytic NO_x Degradation over (Ti,C)-BiOBr/Ti₃C₂T_x MXene Nanocomposites: Role of Ti and C Doping. *Sep. Purif. Technol.* **2021**, *270*, 118815. [[CrossRef](#)]
18. Cao, S.; Shen, B.; Tong, T.; Fu, J.; Yu, J. 2D/2D Heterojunction of Ultrathin MXene/Bi₂WO₆ Nanosheets for Improved Photocatalytic CO₂ Reduction. *Adv. Funct. Mater.* **2018**, *28*, 1800136. [[CrossRef](#)]
19. Sreedhar, A.; Noh, J.S. Recent Advances in Partially and Completely Derived 2D Ti₃C₂ MXene Based TiO₂ Nanocomposites towards Photocatalytic Applications. *Sol. Energy* **2021**, *222*, 48–73. [[CrossRef](#)]
20. Li, Y.; Deng, X.; Tian, J.; Liang, Z.; Cui, H. Ti₃C₂ MXene-Derived Ti₃C₂/TiO₂ Nanoflowers for Noble-Metal-Free Photocatalytic Overall Water Splitting. *Appl. Mater. Today* **2018**, *13*, 217–227. [[CrossRef](#)]
21. Li, Y.; Zhang, D.; Feng, X.; Liao, Y.; Wen, Q.; Xiang, Q. Truncated Octahedral Bipyramidal TiO₂/MXene Ti₃C₂ Hybrids with Enhanced Photocatalytic H₂ Production Activity. *Nanoscale Adv.* **2019**, *1*, 1812–1818. [[CrossRef](#)]
22. Shahzad, A.; Rasool, K.; Nawaz, M.; Miran, W.; Jang, J.; Moztahida, M.; Mahmoud, K.A.; Lee, D.S. Heterostructural TiO₂/Ti₃C₂T_x (MXene) for Photocatalytic Degradation of Antiepileptic Drug Carbamazepine. *Chem. Eng. J.* **2018**, *349*, 748–755. [[CrossRef](#)]
23. Chen, Y.; Li, X.; Cai, G.; Li, M.; Tang, D. In Situ Formation of (0 0 1) TiO₂/Ti₃C₂ Heterojunctions for Enhanced Photoelectrochemical Detection of Dopamine. *Electrochem. Commun.* **2021**, *125*, 106987. [[CrossRef](#)]
24. Xu, Y.; Wang, S.; Yang, J.; Han, B.; Nie, R.; Wang, J.; Wang, J.; Jing, H. In-Situ Grown Nanocrystal TiO₂ on 2D Ti₃C₂ Nanosheets for Artificial Photosynthesis of Chemical Fuels. *Nano Energy* **2018**, *51*, 442–450. [[CrossRef](#)]
25. Hantanasirisakul, K.; Gogotsi, Y. Electronic and Optical Properties of 2D Transition Metal Carbides and Nitrides (MXenes). *Adv. Mater.* **2018**, *30*, 1804779. [[CrossRef](#)] [[PubMed](#)]

26. Alhabeab, M.; Maleski, K.; Anasori, B.; Lelyukh, P.; Clark, L.; Sin, S.; Gogotsi, Y. Guidelines for Synthesis and Processing of Two-Dimensional Titanium Carbide ($\text{Ti}_3\text{C}_2\text{T}_x$ MXene). *Chem. Mater.* **2017**, *29*, 7633–7644. [[CrossRef](#)]
27. Yang, H.G.; Sun, C.H.; Qiao, S.Z.; Zou, J.; Liu, G.; Smith, S.C.; Cheng, H.M.; Lu, G.Q. Anatase TiO_2 Single Crystals with a Large Percentage of Reactive Facets. *Nature* **2008**, *453*, 638–641. [[CrossRef](#)]
28. Yang, C.; Tan, Q.; Li, Q.; Zhou, J.; Fan, J.; Li, B.; Sun, J.; Lv, K. 2D/2D Ti_3C_2 MXene/ $g\text{-C}_3\text{N}_4$ Nanosheets Heterojunction for High Efficient CO_2 Reduction Photocatalyst: Dual Effects of Urea. *Appl. Catal. B Environ.* **2020**, *268*, 118738. [[CrossRef](#)]
29. Zhang, C.J.; Pinilla, S.; McEvoy, N.; Cullen, C.P.; Anasori, B.; Long, E.; Park, S.H.; Seral-Ascaso, A.; Shmeliov, A.; Krishnan, D.; et al. Oxidation Stability of Colloidal Two-Dimensional Titanium Carbides (MXenes). *Chem. Mater.* **2017**, *29*, 4848–4856. [[CrossRef](#)]
30. Naguib, M.; Mashtalir, O.; Lukatskaya, M.R.; Dyatkin, B.; Zhang, C.; Presser, V.; Gogotsi, Y.; Barsoum, M.W. One-Step Synthesis of Nanocrystalline Transition Metal Oxides on Thin Sheets of Disordered Graphitic Carbon by Oxidation of MXenes. *Chem. Commun.* **2014**, *50*, 7420–7423. [[CrossRef](#)]
31. Liu, S.; Yu, J.; Jaroniec, M. Anatase TiO_2 with Dominant High-Energy {001} Facets: Synthesis, Properties, and Applications. *Chem. Mater.* **2011**, *23*, 4085–4093. [[CrossRef](#)]
32. Diebold, U. The Surface Science of Titanium Dioxide. *Surf. Sci. Rep.* **2002**, *48*, 53–229. [[CrossRef](#)]
33. Li, X.; Wu, X.; Liu, S.; Li, Y.; Fan, J.; Lv, K. Effects of Fluorine on Photocatalysis. *Chin. J. Catal.* **2020**, *41*, 1451–1467. [[CrossRef](#)]
34. Rakhi, R.B.; Ahmed, B.; Hedhili, M.N.; Anjum, D.H.; Alshareef, H.N. Effect of Postetch Annealing Gas Composition on the Structural and Electrochemical Properties of Ti_2CT_x MXene Electrodes for Supercapacitor Applications. *Chem. Mater.* **2015**, *27*, 5314–5323. [[CrossRef](#)]
35. Li, B.; Zhao, Z.; Gao, F.; Wang, X.; Qiu, J. Mesoporous Microspheres Composed of Carbon-Coated TiO_2 Nanocrystals with Exposed {001} Facets for Improved Visible Light Photocatalytic Activity. *Appl. Catal. B Environ.* **2014**, *147*, 958–964. [[CrossRef](#)]
36. Ye, M.; Wang, X.; Liu, E.; Ye, J.; Wang, D. Boosting the Photocatalytic Activity of P25 for Carbon Dioxide Reduction by Using a Surface-Alkalinized Titanium Carbide MXene as Cocatalyst. *ChemSusChem* **2018**, *11*, 1606–1611. [[CrossRef](#)]
37. Wang, K.; Li, X.; Wang, N.; Shen, Q.; Liu, M.; Zhou, J.; Li, N. Z-Scheme Core-Shell meso- $\text{TiO}_2@Zn\text{In}_2\text{S}_4/\text{Ti}_3\text{C}_2$ MXene Enhances Visible Light-Driven CO_2 -to- CH_4 Selectivity. *Ind. Eng. Chem. Res.* **2021**, *60*, 8720–8732. [[CrossRef](#)]
38. Li, J.; Huang, H.; Xue, W.; Sun, K.; Song, X.; Wu, C.; Nie, L.; Li, Y.; Liu, C.; Pan, Y.; et al. Self-Adaptive Dual-Metal-Site Pairs in Metal-Organic Frameworks for Selective CO_2 Photoreduction to CH_4 . *Nat. Catal.* **2021**, *4*, 719–729. [[CrossRef](#)]
39. Huo, Y.; Zhang, J.; Dai, K.; Li, Q.; Lv, J.; Zhu, G.; Liang, C. All-Solid-State Artificial Z-Scheme Porous $g\text{-C}_3\text{N}_4/\text{Sn}_2\text{S}_3$ -DETA Heterostructure Photocatalyst with Enhanced Performance in Photocatalytic CO_2 Reduction. *Appl. Catal. B Environ.* **2019**, *241*, 528–538. [[CrossRef](#)]
40. Di, J.; Chen, C.; Yang, S.Z.; Chen, S.; Duan, M.; Xiong, J.; Zhu, C.; Long, R.; Hao, W.; Chi, Z.; et al. Isolated Single Atom Cobalt in $\text{Bi}_3\text{O}_4\text{Br}$ Atomic Layers to Trigger Efficient CO_2 Photoreduction. *Nat. Commun.* **2019**, *10*, 2840. [[CrossRef](#)]
41. Xia, P.; Zhu, B.; Yu, J.; Cao, S.; Jaroniec, M. Ultra-Thin Nanosheet Assemblies of Graphitic Carbon Nitride for Enhanced Photocatalytic CO_2 Reduction. *J. Mater. Chem. A* **2017**, *5*, 3230–3238. [[CrossRef](#)]
42. Jiao, X.; Li, X.; Jin, X.; Sun, Y.; Xu, J.; Liang, L.; Ju, H.; Zhu, J.; Pan, Y.; Yan, W.; et al. Partially Oxidized SnS_2 Atomic Layers Achieving Efficient Visible-Light-Driven CO_2 Reduction. *J. Am. Chem. Soc.* **2017**, *139*, 18044–18051. [[CrossRef](#)] [[PubMed](#)]
43. Li, X.; Sun, Y.; Xu, J.; Shao, Y.; Wu, J.; Xu, X.; Pan, Y.; Ju, H.; Zhu, J.; Xie, Y. Selective Visible-Light-Driven Photocatalytic CO_2 Reduction to CH_4 Mediated by Atomically Thin CuIn_5S_8 Layers. *Nat. Energy* **2019**, *4*, 690–699. [[CrossRef](#)]
44. Xiao, N.; Li, S.; Liu, S.; Xu, B.; Li, Y.; Gao, Y.; Ge, L.; Lu, G. Novel PtPd Alloy Nanoparticle-Decorated $g\text{-C}_3\text{N}_4$ Nanosheets with Enhanced Photocatalytic Activity for H_2 Evolution under Visible Light Irradiation. *Chin. J. Catal.* **2019**, *40*, 352–361. [[CrossRef](#)]
45. Wang, Z.; Lv, K.; Wang, G.; Deng, K.; Tang, D. Study on the Shape Control and Photocatalytic Activity of High-Energy Anatase Titania. *Appl. Catal. B Environ.* **2010**, *100*, 378–385. [[CrossRef](#)]
46. Xia, Y.; Cheng, B.; Fan, J.; Yu, J.; Liu, G. Unraveling Photoexcited Charge Transfer Pathway and Process of CdS/Graphene Nanoribbon Composites toward Visible-Light Photocatalytic Hydrogen Evolution. *Small* **2019**, *15*, 1902459. [[CrossRef](#)]
47. Neațu, Ș.; Maciá-Agulló, J.A.; Concepción, P.; Garcia, H. Gold-Copper Nanoalloys Supported on TiO_2 as Photocatalysts for CO_2 Reduction by Water. *J. Am. Chem. Soc.* **2014**, *136*, 15969–15976. [[CrossRef](#)]
48. Li, Y.; Yin, Z.; Ji, G.; Liang, Z.; Xue, Y.; Guo, Y.; Tian, J.; Wang, X.; Cui, H. 2D/2D/2D Heterojunction of Ti_3C_2 MXene/ MoS_2 Nanosheets/ TiO_2 Nanosheets with Exposed (001) Facets toward Enhanced Photocatalytic Hydrogen Production Activity. *Appl. Catal. B Environ.* **2019**, *246*, 12–20. [[CrossRef](#)]
49. Li, Y.; Ding, L.; Liang, Z.; Xue, Y.; Cui, H.; Tian, J. Synergetic Effect of Defects Rich MoS_2 and Ti_3C_2 MXene as Cocatalysts for Enhanced Photocatalytic H_2 Production Activity of TiO_2 . *Chem. Eng. J.* **2020**, *383*, 123178. [[CrossRef](#)]
50. Li, Y.; Ding, L.; Yin, S.; Liang, Z.; Xue, Y.; Wang, X.; Cui, H.; Tian, J. Photocatalytic H_2 Evolution on TiO_2 Assembled with Ti_3C_2 MXene and Metallic 1T- WS_2 as Co-Catalysts. *Nano-Micro Lett.* **2020**, *12*, 1–12. [[CrossRef](#)]
51. Zhang, X.; Nie, J.; Rao, F.; Liu, H.; Wang, Y.; Qu, D.; Wu, W.; Zhong, P.; Zhu, G. $\text{Ti}_3\text{C}_2@/\text{TiO}_2/g\text{-C}_3\text{N}_4$ Heterojunction Photocatalyst with Improved Charge Transfer for Enhancing Visible-Light NO Selective Removal. *Ceram. Int.* **2021**, *47*, 31302–31310. [[CrossRef](#)]